



Abrupt transition from natural to anthropogenic aerosol radiative forcing: Observations at the ABC-Maldives Climate Observatory

M. V. Ramana¹ and V. Ramanathan¹

Received 6 January 2006; revised 8 May 2006; accepted 26 June 2006; published 25 October 2006.

[1] Using aerosol-radiation observations over the north Indian Ocean, we show how the monsoon transition from southwest to northeast flow gives rise to a similar transition in the direct aerosol radiative forcing from natural to anthropogenic forcing. These observations were taken at the newly built aerosol-radiation-climate observatory at the island of Hanimaadhoo (6.776°N, 73.183°E) in the Republic of Maldives. This observatory is established as a part of Project Atmospheric Brown Clouds (ABC) and is referred to as the ABC-Maldives Climate Observatory at Hanimaadhoo (ABC_MCOH). The transition from the southwest monsoon during October to the northeast monsoon flow during early November occurs abruptly over a period of few weeks over ABC-MCOH and reveals a dramatic contrast between the natural marine aerosols transported from the south Indian Ocean by the southwest monsoon and that of the polluted aerosols transported from the south and Southeast Asian region by the northeast monsoon. We document the change in the microphysical properties and the irradiance at the surface, to identify the human signature on aerosol radiative forcing. We first establish the precision of surface radiometric observations by comparing simultaneous observations using calibrated Kipp & Zonen and Eppley pyrhemometers and pyranometers for direct, diffuse and global solar radiation. We show that the direct, diffuse and global radiation can be measured within a precision of about 3 to 5 Wm^{-2} . Furthermore, when we include the observed aerosol optical properties as input into the Monte Carlo Aerosol Cloud Radiation (MACR) model (developed by us using Indian Ocean Experiment data), the simulated fluxes agree with the observed direct, diffuse and global fluxes within the measurement accuracy. A steady southwest monsoon flow of about 5 to 7 ms^{-1} persists until middle of October which switches to an abrupt change in direction to northeast flow of similar speeds bringing in polluted air from south Asia. However, it is not until end of November that a steady northeasterly flow is well established. The abrupt transition is accompanied by a large increase in aerosol optical depth from about 0.1 in October to as high as 0.4 during January, the SSA decreases from 1 to about 0.9, and the Angstrom coefficient increases from about 0.5 (suggesting large particles > 1 micron) to about 1.2 in January (submicron particles) and an increase in aerosol extinction below 3 km altitude. These changes are consistent with the transport of continental pollution from south and Southeast Asia (about 1000 to several 1000 km away from ABC_MCOH) to the north Indian Ocean during the northeast monsoon. The direct aerosol forcing, determined solely from radiometric observations without resorting to models, changes from -5 Wm^{-2} during October to -22 Wm^{-2} during January. About 50% of this forcing occurs in the photosynthetically active part of the solar spectrum (0.4 to 0.7 micron). MACR shows that the decrease in SSA from 1 to 0.9 changes the aerosol forcing efficiency by a factor of about 2 from about -40 Wm^{-2} (per AOD) in October to -80 Wm^{-2} (per AOD) in January. Thus the arrival of the brown clouds from south and Southeast Asia has a large seasonal dimming effect over remote parts of the north Indian Ocean. The observational results presented here should be used for validating climate models that attempt to simulate the anthropogenic effects of aerosol forcing on climate. The observational and model results presented in this study shows how near continuous surface based observations can be used to differentiate the human impact on aerosol forcing which is a major challenge for models.

¹Center for Atmospheric Sciences, Scripps Institution of Oceanography, University of California, San Diego, La Jolla, California, USA.

Citation: Ramana, M. V., and V. Ramanathan (2006), Abrupt transition from natural to anthropogenic aerosol radiative forcing: Observations at the ABC-Maldives Climate Observatory, *J. Geophys. Res.*, *111*, D20207, doi:10.1029/2006JD007063.

1. Introduction

[2] The Project Atmospheric Brown Cloud (ABC) is an international research effort initiated by the United Nations Environment Programme (UNEP) and its current focus is on the Asia-Pacific region [Ramanathan and Crutzen, 2003]. Project ABC is built upon the Indian Ocean Experiment (INDOEX) completed in 1998–1999 [Ramanathan et al., 2001], which was confined to a particular season (Northern Hemispheric winter season) and region (tropical Indian Ocean). This project seeks to answer the major environmental challenges facing the Indo-Asia-Pacific region in the coming decades, specifically the environmental consequences of raising air pollution levels due to rapid industrialization and population growth [Ramanathan and Ramana, 2003]. The project includes the construction of about 12 aerosol-radiation-climate observatories (<http://www-abc-asia.ucsd.edu>) in the Indo-Asian-Pacific region to perform long-term measurements of the chemistry and microphysics of aerosol and solar radiation. Toward this goal, the first ABC aerosol-radiation-climate observatory is constructed and installed with aerosol and radiation instruments at Hanimaadhoo Island (Republic of Maldives) which is located in the tropical Indian Ocean. This observatory is referred to as ABC-Maldives Climate Observatory in Hanimaadhoo (ABC_MCOH).

[3] The region is characterized by a tropical monsoon climate with a seasonal reversal of winds and a distinct seasonality of precipitation. The seasonal classification followed by Indian meteorologists and agriculturalists are given in Table 1 [Kumar et al., 2004; Kripalani and Kumar, 2004]. During the summer monsoon season (June–September), winds flow from the Southern Hemisphere toward the Indian subcontinent as a southwesterly flow, accumulating moisture and depositing copious amounts of precipitation over India and the surrounding regions. The anthropogenic aerosol loading over south Asia builds up during winter (December–February) and premonsoon (March–May) dry seasons in the presence of a stable boundary layer inversion and transports pollutants by low-level northeasterly winds from south and Southeast Asia and surrounding areas toward the Arabian Sea and the north Indian Ocean. October is the month of transition between the wet and dry monsoon seasons where winds in northern Indian Ocean and the Arabian sea changes from southwesterly during June–September to northerly and northeasterly winds, bringing aerosols from much of south and Southeast Asia to the Arabian Sea, Bay of Bengal, and north Indian Ocean.

[4] The MCOH was inaugurated with the ABC Post-Monsoon Experiment (APMEX; <http://www-abc-asia.ucsd.edu/APMEX/october2004campaign.htm>) to understand the atmospheric aerosols and regional haze from air pollution and their effect on the solar irradiance reaching the surface during the post-monsoon season. The APMEX was conducted from 1 October 2004 to 15 November 2004 with intensive observations using instruments installed at the Hanimaadhoo observatory, and instruments installed on manned and unmanned aircraft vehicles. Data are being collected at ABC_MCOH in real time on a continuous basis since 1 October 2004.

[5] The first objective of this paper is to establish the precision of pyrhelimeter and pyranometer measurements in warm and humid regimes. Our next objective is to establish how the monsoon transition influences aerosol physical properties and the radiative forcing. Lastly, we adopt the observed aerosol physical properties and optical depths in a Monte Carlo Aerosol Radiation Model (MACR) and estimate the solar fluxes and the aerosol direct forcing. The estimated fluxes and forcing values are validated with observed values and the model is subsequently used to understand the basic parameters that govern the modulation of the forcing by the monsoon flow.

2. Experimental Setup and Instrumentation

[6] The Republic of Maldives is a long chain of coral atolls in the Indian Ocean that extends for 800 km north to south from near the tip of India to the equator (see Figure 1a). Hanimaadhoo is a coral reef island located within the northernmost atolls of the Maldives (6.776°N, 73.183°E) and the island measures ~4.0 km long (north-south) by ~1.0 km wide (east-west). The population of the island is ~1200 and is free from major landmass as well as immediate local effects such as infrastructure, industries, local pollution, local orography and heat island. The tiny island of Hanimaadhoo is selected as the ABC observatory site because of its remoteness from major landmasses as well as other neighboring islands. The MCOH is located at the northern tip of this island (Figure 1b) and this specific location of the observatory is selected such that the prevailing winds come from over the ocean, thus avoiding local pollution generated by the few inhabitants of Hanimaadhoo. The MCOH is down wind of the Indian subcontinent during the dry season and upwind of the subcontinent during the wet season. The predominant circulation in this region, from October to April, consists of low-level northeasterlies. From June to September (southwest monsoon), the surface flow reverses from northeasterlies to southwesterlies. Thus MCOH is located at an ideal location to facilitate observations in the northeast and southwest monsoons, as well as the transitional periods between them. This site has instruments making continuous measurements of broadband, narrowband and spectral irradiances, spectral aerosol optical depths, vertical profiles of aerosols, near-surface aerosol chemical and optical properties and meteorological parameters. All of the radiometric and meteorological instruments are mounted on the top of a 15-m tower to have a hemispherical field of view free of interferences by trees (Figures 1c and 1d show photos of the observatory and field of view from the tower). A list of instruments installed at MCOH is listed in Table 2 along with their specifications and their installation details are given below. These set of instruments enables the simultaneous measurements of aerosol characteristics and radiative fluxes reaching the Earth's surface.

2.1. Radiometric Measurements

[7] Pyrhemimeters (Kipp & Zonen and Eppley make) and ventilated pyranometers (CM 21 and CM 22 of Kipp & Zonen) are mounted on a Kipp & Zonen model 2AP-GD

Table 1. Classification of Seasonal Periods as Employed by Indian Meteorologists and Agriculturalists

Period	Classification Based on Earth Orbiting Around the Sun	Classification Based on Seasonal Reversal of Winds	Classifications Based on Cultivation	Classification Based on Rainfall
Jun–Sep	summer	southwest (SW) monsoon or summer monsoon	Kharif	southwest monsoon
Oct–Nov	autumn	postmonsoon or retreating SW monsoon	Rabi or Kharif harvest	Oct–Dec: NE monsoon
Dec–Feb	winter	northeast (NE) monsoon or winter monsoon	Rabi	Jan–Feb: winter
Mar–May	spring	premonsoon	harvest	premonsoon

two-axis Sun tracker to measure the ground reaching direct and diffuse solar fluxes respectively. The Sun tracker is equipped with Sun sensor, pointing, and shading ball assembly. The Sun sensor provides active Sun tracking capability (active correction to both time and position) for indefinite unattended operation. The pointing and shading ball assembly provides mountings for three diffuse (shaded pyranometers) and three direct (pyrheliometers) radiometers. The diameter of the shading ball is 5.72 cm and is at about 69 cm from the center of the pyranometer detector. Three pyrheliometers; 1 from Kipp & Zonen and 2 from Eppley, are used to measure direct solar fluxes in the wavelength range from 0.2 to 4.0 μm , which results from the radiant flux from a solid angle of 5° . The Kipp & Zonen pyrheliometer (CH1 type) has quartz window; whereas Eppley pyrheliometers has quartz and Calcium Fluoride (CaF_2) windows. The absolute accuracy of these instruments is $\pm 1\%$, with a precision of about 1% per year. Two ventilated pyranometers; namely CM 21 and CM 22 of Kipp & Zonen pyranometers, are used to measure the ground reaching diffuse solar radiation. The CM 21 and CM 22 type pyranometers respectively measures irradiance in the wavelength range of 0.3–2.8 μm and 0.2–3.6 μm on a plane surface. These instruments does not exhibit tilt dependence thus they can measure solar radiation at high solar zenith angles as well. The absolute accuracy of these instruments is about ± 1 –2%. The ground reaching global solar flux (direct + diffuse) is measured using another ventilated pyranometer, CM 21 of Kipp & Zonen, by not shading the sensor. All the pyranometers are ventilated with CV 2 type Kipp & Zonen ventilation unit. The down welling infrared radiation in the 4.5 to 42.0 μm wavelength range is measured using a ventilated pyrgeometer (CG4 type of Kipp & Zonen) by shading it from the direct beam irradiance using the same Sun tracker and shading ball assembly. The data from these instruments were sampled continuously at 10 s interval.

[8] The photodiode flux radiometer (GUV-2511 type), manufactured by Biospherical Instrument Inc. (BSI), is installed on the top of the tower to measure the ground reaching global irradiance in six 10 nm wide bands at 305, 313, 320, 340, 380 and 395 nm and broad visible band at 400–700 nm (Photosynthetically Active Radiation). This instrument has been factory calibrated and the data are sampled at 1 s interval. The accuracy in the measurement of clear-sky global irradiance is 2.4% and the precision ranges from 0.2% to 2.0%. The angular, spectral, and absolute response characteristics of the instrument are described in detail by Conant [2000]. All the radiometers (glass domes and diffusers) are cleaned daily before the sunrise and are periodically checked to ensure that the instruments are leveled in horizontal plan. Standard Meteorological instruments from R.M. Young Company are

installed on the top of the 15 m tower to monitor wind speed, wind direction, air temperature, relative humidity, pressure and rainfall and the data from these instruments are sampled at 10 s interval. All of the above instruments were purchased just before the start of this study with factory calibration.

2.2. Columnar Aerosol Measurements

[9] Measuring aerosol spectral optical depths, columnar ozone and columnar precipitable water vapor are very important because the solar radiation reaching the ground is attenuated by absorption and scattering by atmospheric molecules as well as aerosols. These parameters are measured using two different types of Sun photometers, namely, Microtops II Sun photometer (Solar Light Company, Philadelphia, USA) and using CIMEL sky radiometer (AERONET, National Aeronautics and Space Administration (NASA), Maryland, USA).

[10] Two handheld Microtops II (Sun photometer and Ozone) with spectral filters for visible and near-infrared wavelengths are used to retrieve aerosol optical depth (AOD), columnar water vapor, and columnar ozone. The AOD is measured at 380, 440, 500, 675, 870 nm by the Sun photometer and at 1020 nm by the Ozone and the columnar water vapor (at 940 nm) and ozone (at 305, 312, 320 nm) are measured by the Ozone. These observations are performed manually with Sun photometer and Ozone under clear-sky conditions several times a day. Each Microtops is fitted with 5 collimators with a field of view of 2.5° . These instruments have been purchased (Solar Light Co.) just before the APMEX campaign with calibration certificates and the absolute accuracy of these instruments is about 2% [Morys *et al.*, 2001]. The CIMEL sky radiometer is installed at MCOH during November 2004 on the top of the tower with no obstruction to Sun to measure aerosol properties, as a part of the Aerosol Robotic Network (AERONET) archive. The CIMEL radiometer is described in detail by Holben *et al.* [1998] and here briefly explained. The CIMEL sky radiometer is an automatic tracking Sun and sky scanning radiometer with 1.2° field of view and measures aerosol optical depth at seven wavelengths (340, 380, 440, 500, 670, 870, and 1020 nm) and precipitable water vapor at 940 nm. The CIMEL radiometer scans Sun every 15 min and the uncertainty in the AOD measurements is about ± 0.01 –0.02 [Holben *et al.*, 1998; Eck *et al.*, 2001]. This instrument has been calibrated at NASA before installing it.

[11] Vertical profiles of the tropospheric aerosols are measured using a high-resolution (30 m) Micro-Pulse Lidar (MPL) system [Spinhirne *et al.*, 1995]. The MPL laser pulse duration is 10 ns with a pulse repetition frequency of 2500 Hz and its output energy is 5 μJ . This high pulse repetition frequency allows the system to average many low-energy pulses in a short time to achieve a good signal-to-noise ratio.

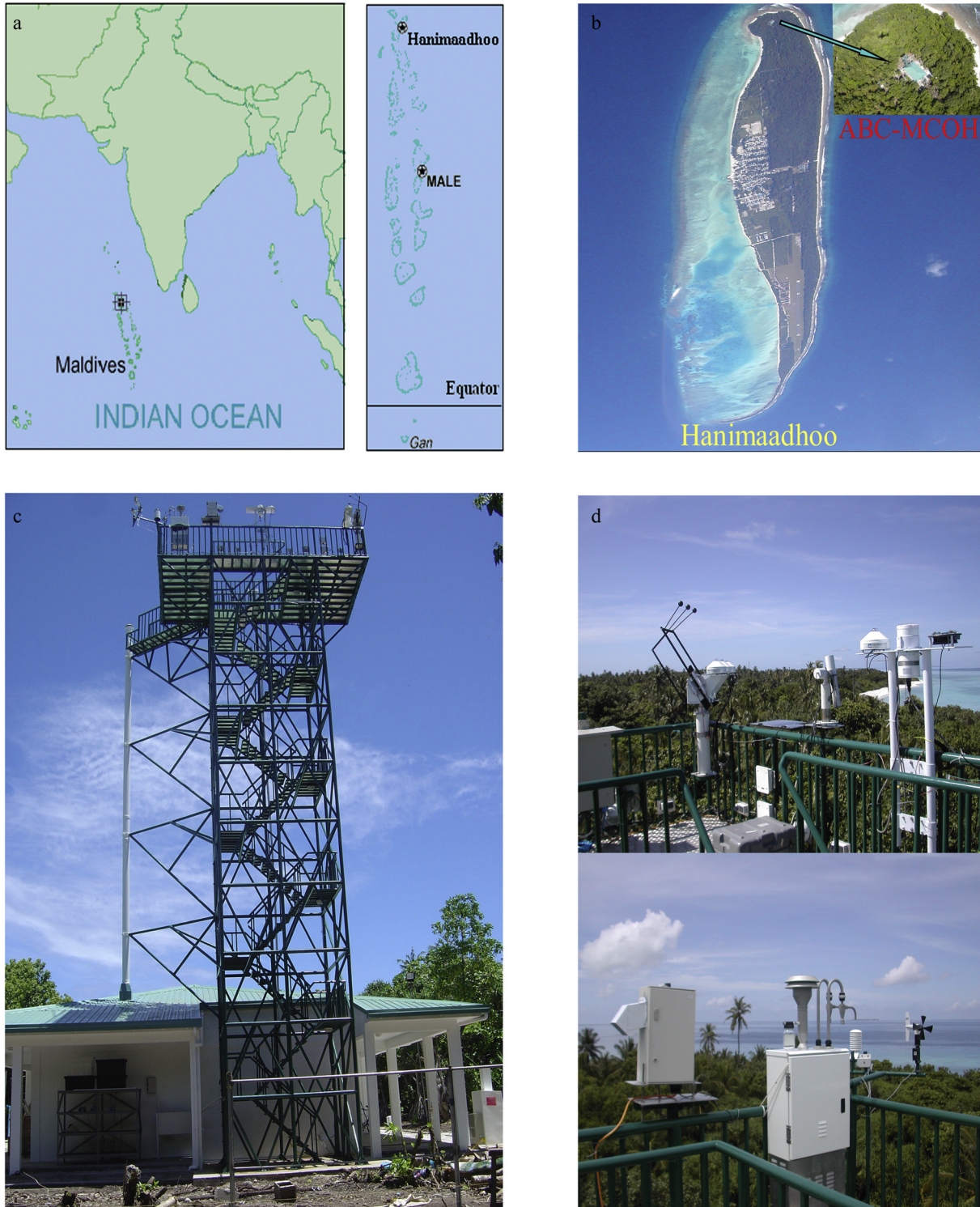


Figure 1. ABC_MCOH observatory. (a) Maps showing the Asian continent and Maldives Island, (b) aerial view of the MCOH observatory at Hanimaadhoo Island, (c) photo of the 15-m-tower at MCOH, and (d) radiation instruments installed on the tower.

The MPL has been installed inside a climate-controlled housing with a glass window on the roof and is operated continuously during the daytime except during raining and overcast conditions. The MPL returned signals have been

averaged and stored at 1-min time interval from the surface up to an altitude of 60 km. In addition to the above mentioned instruments, different kinds of aerosol instruments are installed at MCOH to measure the aerosol size distribution,

Table 2. Instruments Deployed at ABC_MCOH

Parameter	Instrument Type, Manufacturer	Accuracy
Diffuse solar radiation	CM 21 Pyranometer (0.3–2.8 μm), Kipp & Zonen	$\sim\pm 2\%$
Diffuse solar radiation	CM 22 Pyranometer (0.2–3.6 μm), Kipp & Zonen	$\sim\pm 1\%$
Global solar radiation	CM 21 Pyranometer (0.3–2.8 μm), Kipp & Zonen	$\sim\pm 2\%$
Direct solar radiation	CH1 Pyrheliometer (0.2–4.0 μm), Kipp & Zonen;	$\pm 1\%$
Direct solar radiation	Pyrheliometer with Quartz window, Eppley; Pyrheliometer with Calcium Florid window, Eppley	$\pm 1\% \pm 1\%$
Net radiation in the far infrared	CG4 Pyrgeometer (4.5–42.0 μm), Kipp & Zonen	$\pm 3\%$
Sun tracking	2AP-GD Sun tracker with Sun sensor, pointing and shading ball assembly, Kipp & Zonen	$\pm 0.05^\circ$
Global PAR	Narrowband radiometer GUV-2511 (0.305, 0.313, 0.32, 0.34, 0.38, 0.395, 0.4–0.7 μm), Bio-Spherical Instruments	$\pm 2.4\%$
Aerosol spectral optical depth, columnar precipitable water vapor	Microtops II Sun photometer (AOD at 380, 440, 500, 675, 870, 1020 nm; PWV at 940 nm), Solar Light Co.	± 0.02
Aerosol spectral optical depth, columnar precipitable water vapor	CIMEL Sun photometer (AOD at 340, 380, 440, 500, 670, 870, 1020 nm; PWV at 940 nm), AERONET	± 0.01 –0.02
Columnar ozone	Microtops II Ozonometer (305, 312, 320 nm), Solar Light Co.	± 1 –2%
Aerosol vertical profiles	Micro pulse Lidar, at 523 nm, Science and Engineering Services Inc.	$\sim\pm 0.005 \text{ km}^{-1}$
Wind speed and direction, temperature, humidity, pressure, rainfall	R. M. Young Company instruments	$\pm 0.2 \text{ ms}^{-1}$, ± 3 degrees, $\pm 0.3^\circ\text{C}$, $\pm 2\%$ RH, $\pm 0.5 \text{ mb}$, ± 2 –3%

chemical composition, number density, absorption and scattering measurements etc., and are described by *Corrigan et al.* [2006].

3. Precision of Radiometric Measurements

[12] The period of data analyzed for this work is from 1 October 2004 to 31 January 2005 and thus it covers the monsoon transition period and the north east monsoon. First, we will establish the precision of the solar flux measurements.

3.1. Broadband Solar Fluxes

[13] The flux data are screened for clouds to pick out clear sky fluxes following the procedure described by *Conant* [2000]. Figures 2a–2c show the comparisons of direct solar flux measurements using Kipp & Zonen and Eppley pyrheliometers. The Kipp & Zonen pyrheliometer has quartz window whereas Eppley type pyrheliometers has quartz and calcium fluoride windows. All these pyrheliometers have 5° of field of view and measure the direct component of the shortwave radiation in the 0.2–4.0 μm wavelength range. The Eppley made quartz and CaF_2 window pyrheliometers (Figure 2a) agree within 1.27 Wm^{-2} , with a root mean square error (RMSE) of 1.68 Wm^{-2} and a slope of 0.99. The zero offset is only 0.19 Wm^{-2} . The maximum difference of 2.56 Wm^{-2} was seen between the Kipp & Zonen pyrheliometer with quartz window and the Eppley quartz window pyrheliometer (Figure 2b). The Eppley made CaF_2 window pyrheliometer (Figure 2c) agrees with the Kipp & Zonen within 1.22 Wm^{-2} with a root mean square error (RMSE) of 2.39 Wm^{-2} and a slope of 0.99. In view of the close agreement between the three radiometers, we can conclude that the three radiometers agree within 3 Wm^{-2} (or within 0.5%) and our absolute precision is also of this order. In general, these differences are consistent with the instrumental uncertainties ($\pm 1\%$).

[14] Before installing Kipp & Zonen CM 21 type pyranometers for global (unshaded) and diffuse (shaded) measurements, both radiometers were directly compared for

1 week while measuring global radiation. Since both radiometers are of the same make and model, nearly identical results were expected. This technique is meant to identify and characterize the small deviations that exist even between identical instruments. Figure 2d shows the scatterplot of global flux measurements made with two CM 21 type ventilated pyranometers. Both the pyranometers agree within 0.76 Wm^{-2} and have an RMSE of 0.87 Wm^{-2} and a slope of 0.99 (zero offset is 0.01 Wm^{-2}). The data from these two pyranometers are nearly identical which demonstrates that measurements are reproducible to about less than 1 Wm^{-2} . Figure 2e shows the scatterplot of the diffuse flux measured with CM 21 ventilated pyranometer against those with CM 22 ventilated pyranometer. The CM 21 and CM 22 type pyranometers respectively measures the ground reaching diffuse solar radiation in the 0.3–2.8 μm and 0.2–3.6 μm wavelength range. These two types of pyranometers are compared to evaluate the ground reaching radiation over these wavelengths, since most of the observatories around the world are equipped with CM 21 type pyranometer. In addition, most researchers derive the diffuse flux by subtracting the direct flux (0.2–4.0 μm) measurements from the global flux (0.3–2.8 μm) measurements. The CM 22 type pyranometer slightly over estimates the CM 21 pyranometer: the mean bias is 2.79 Wm^{-2} , RMSE is 3.29 Wm^{-2} , slope is 1.03, and zero offset is 0.18 Wm^{-2} . However, the exact comparison of diffuse radiation measurements requires corrections to the measurements due to shadow ball and wavelength (to compare at same wavelengths) which is discussed in section 5.

3.2. Comparison of AOD Retrievals With Microtops and CIMEL

[15] The aerosol optical depths at 500 nm, common to both of the instruments Microtops and CIMEL Sun photometers, are investigated here using the data collected during December 2004 and January 2005. Figure 3 shows a scatterplot of the AODs measured directly with Microtops against those of the CIMEL Sun photometer. The data points displayed in Figure 3 correspond to times that are tagged as cloud-screened and are measured within 10 min

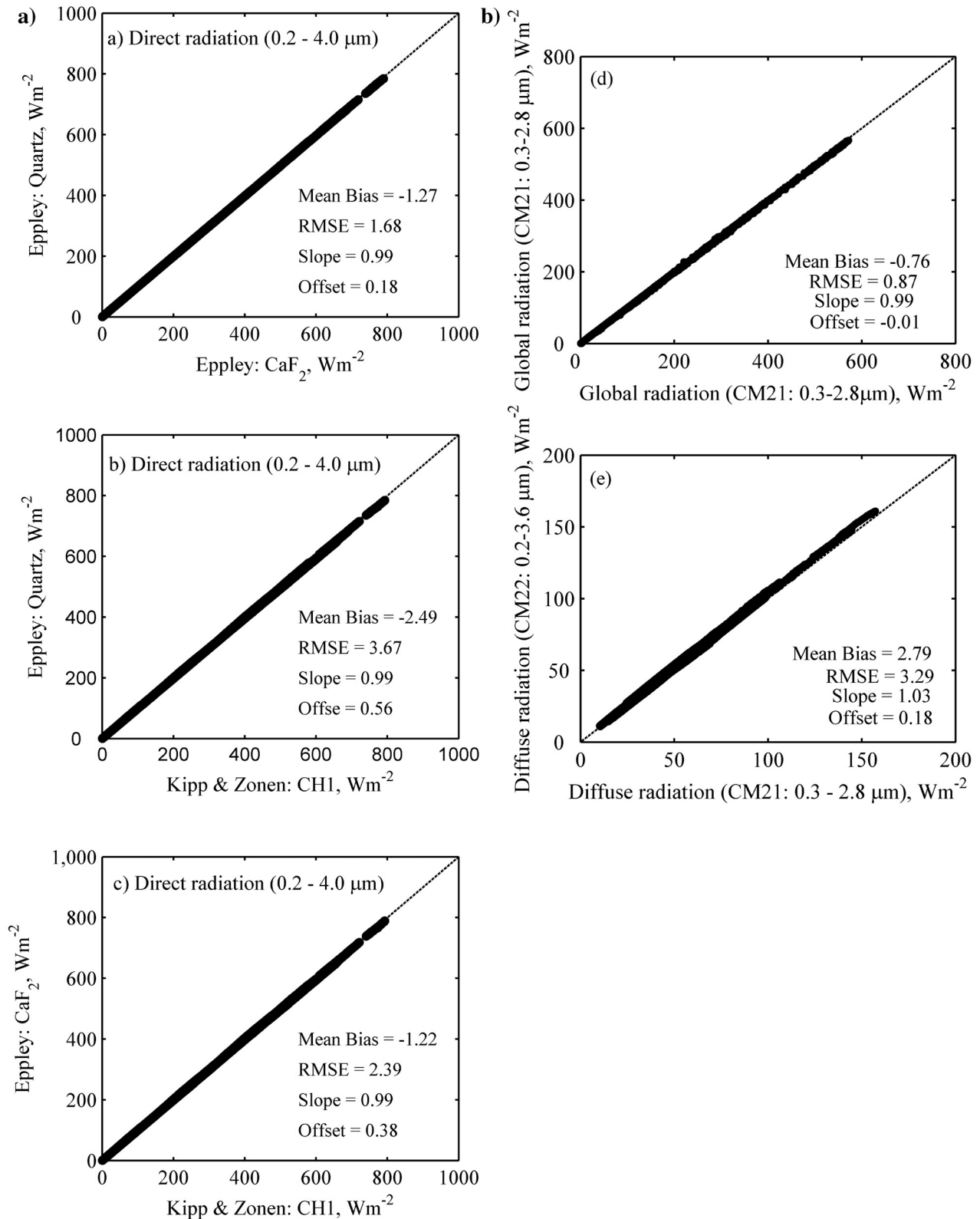


Figure 2. Scatterplot of the (a) comparison of direct solar radiation measured by two Eppley pyrheliometers (Calcium florid window versus quartz window), (b) comparison of direct solar radiation using Kipp & Zonen CH1 quartz window and Eppley type quartz window pyrheliometers, (c) comparison of direct solar radiation measured using Kipp & Zonen CH1 type and Eppley type Calcium Florid window pyrheliometers, (d) comparison of global solar radiation by CM 21 type Kipp & Zonen pyranometers, and (e) comparison of diffuse solar radiation by CM 21 & CM 22 Kipp & Zonen pyranometers. The dashed line corresponds to perfect agreement.

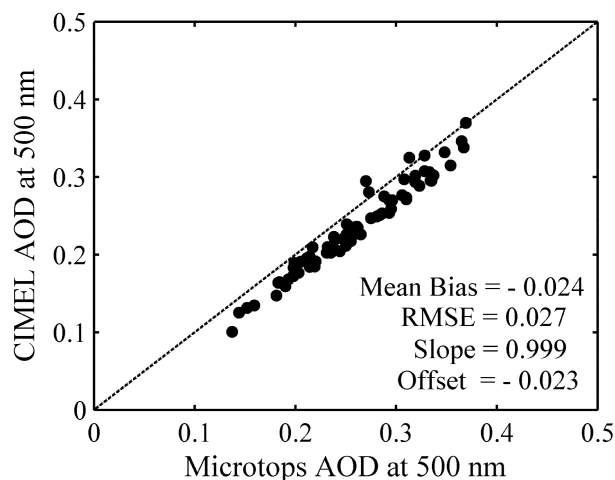


Figure 3. Scatterplot of the measured aerosol optical depth (AOD) at 500 nm for the CIMEL and Microtops instruments. The dashed line corresponds to perfect agreement.

time interval. The Microtops seem to over estimate AOD slightly with respect to AERONET at 500 nm (Figure 3). The slope is close to 1 (0.999); the zero offset is -0.023 ; and the mean bias is -0.024 with an RMSE of 0.027. The uncertainty in AOD measurements is within 0.02 and similar differences were documented previously [Ichoku *et al.*, 2002; Dubovik *et al.*, 2000]. These small differences are inherent to the small differences between the instrument electronics and are within the instrumental uncertainties.

4. Monsoon Transition and Its Influence on Observed Aerosol Characteristics

4.1. Monsoonal Flow Transition

[16] The monthly mean regional flow patterns for October to January are shown in Figures 4a–4d for the near surface winds (1000 mb) and in Figures 4e–4h for the 700 mb region based on the NCEP/NCAR reanalysis streamlines data. In general over MCOH, the regional flow at the surface during October moves from Southern Hemisphere (SH) to Northern Hemisphere (NH) as southwesterly, whereas from November to January the flow moves from NH to SH as northeasterly. At 700 mb, the wind direction over MCOH is consistently from east or north. The variations of daily mean wind direction and speed measured at MCOH are shown in Figures 5a and 5b. The surface winds are mainly westerlies or southwesterlies until 19 October 2004 followed by the sudden reversal of easterly to north easterly flow in about few days. The surface wind fluctuates between westerlies to easterlies first week of November. From then on the easterlies to north easterlies take over with the exception of one westerly event during the third week of November. The seasonal segregation, i.e., namely southwest monsoon, transition, and northeast monsoon are employed on the basis of the changes in the wind direction criteria and are shown in Figure 5a. The mean wind speeds varied from less than a meter per second to 6 ms^{-1} and most of the time the wind speeds are low in the range 2 to 4 ms^{-1} . There are also some relatively calm conditions in which wind speeds are less than 0.5 ms^{-1} as well as

some occasional higher wind speeds reaching 8 ms^{-1} . Figures 5c and 5d show the daily mean variation of surface specific humidity (q in g Kg^{-1}) and columnar precipitable water vapor (PWV in cm). It is seen from these figures that the surface specific humidity ranged from 14 to 15 g Kg^{-1} (relative humidity of 80 to 90%) before the transition period (before 19 October) and decreased to 13 to 14 g Kg^{-1} (RH of 70% to 80%) during the northeast monsoon (after 1 December). The surface changes were also reflected in columnar atmospheric water vapor content, which decreased from values exceeding 4 cm during the SW monsoon and transition seasons to less than 3 cm as the NE monsoon progressed bringing dry air.

4.2. Temporal Variability of Aerosol Optical Depth (AOD)

[17] The temporal variation of daily mean AOD at 500 nm from October 2004 to January 2005 at MCOH are shown in Figure 6a. The AOD does not reveal the rapid fluctuations of the surface wind speed (Figure 6a), but instead shows a steady build up of aerosols from the beginning of October. The primary reason is that the build up occurs at all levels from the surface to about 4 km (as shown in Figure 7 to be discussed later) and thus is not subject to the rapid fluctuations of the surface wind speed. Figure 7 basically reveals the large build up with the progression of the dry season. The steep increase in AOD from 0.1 during October 2004 (i.e., during the southwest monsoon) to ~ 0.4 during January 2005 (i.e., during the northeast monsoon) is due to the long-range transport of aerosols from the continents. Similar pattern is revealed in the Angstrom exponent (Figure 6b), which serves as an index for the effective radius of the particles. The Angstrom exponent is a basic measure of the aerosol size distribution (or atmospheric spectral aerosol index) and is defined by the wavelength dependence of aerosol optical depth,

$$\tau_{\lambda} = \beta \lambda^{-\alpha} \quad (1)$$

where α is the Angstrom exponent, β is the turbidity parameter, λ is the wavelength in μm , and τ_{λ} is the aerosol optical depth at λ . Small value of α around zero represents supermicrometer aerosols (large sea salt and dust particles) whereas large value of α around 2.0 represents submicrometer aerosols (small smoke particles) [Dubovik *et al.*, 2002]. The Angstrom exponents were determined from the spectral AODs yielded by Sun photometer measurements. The daily mean values of Angstrom coefficient from October 2004 to January 2005 at MCOH are shown in Figure 6b. The mean value of the Angstrom exponent was low (~ 0.5 ; i.e., larger particles typical of sea salt and dust) during the beginning of October (i.e., during the southwest monsoon) and increased to a mean value of ~ 1.2 by December (i.e., during the northeast monsoon), pointing out the dominance of submicrometer aerosol particles as the prevailing wind changes from southwesterly or westerly to northeasterly or easterly. The mean and standard deviation of AOD and Angstrom exponent values during SW, transition, and NE monsoon seasons are given in Table 3. The high values of AOD and Angstrom exponent during strong northerly winds is a clear indication of long-range transport of pollution aerosols. The

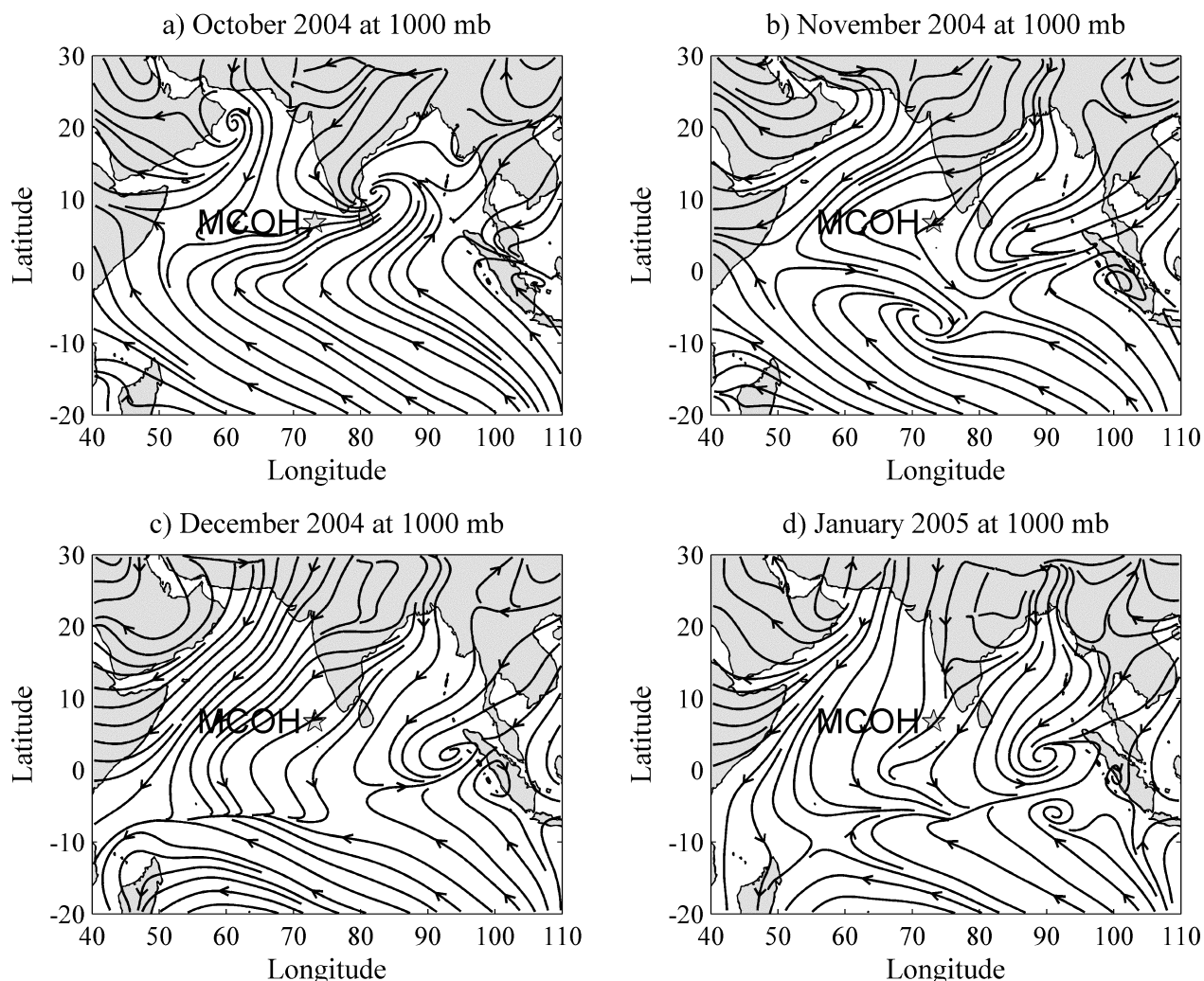


Figure 4. Prevailing monthly mean atmospheric circulation at 1000 mb level during (a) October 2004, (b) November 2004, (c) December 2004, and (d) January 2005 based on NCEP/NCAR reanalysis streamlines data provided by the NOAA-CIRES Climate Diagnostic Center. Prevailing monthly mean atmospheric circulation at 700 mb level during (e) October 2004, (f) November 2004, (g) December 2004, and (h) January 2005 based on NCEP/NCAR reanalysis streamlines data provided by the NOAA-CIRES Climate Diagnostic Center.

increase is also accompanied by an increase in absorption, aerosol size distribution and total number of aerosol particles concentrations [Corrigan *et al.*, 2006].

4.3. Temporal Variability of Aerosol Single Scattering Albedo

[18] Single scattering albedo (SSA) is the ratio of the aerosol scattering coefficient to the total aerosol extinction coefficient (scattering + absorption) and is defined as the fraction of sunlight intercepted by the aerosol that is scattered. SSA is derived from the simultaneous scattering and absorption measurements at 450, 550 and 700 nm. The scattering and absorption were measured under ambient conditions using a TSI 3563 3-wavelength nephelometer and a Magee Scientific AE-31 7-wavelength aethalometer. The scattering coefficients are taken directly from the instrumental data and corrected using Anderson and Ogren [1998]. The absorption coefficients are derived from the

aethalometer data using the method outlined in Arnott *et al.* [2005]. Further details of these measurements are given by Corrigan *et al.* [2006]. SSA at 500 nm is retrieved from the spectral SSA at 450 nm and 550 nm using equation (1) (by substituting SSA for AOD). Figure 6c shows the temporal variation of 12-hour average (daytime and nighttime averages) of SSA at 500 nm from October 2004 to January 2005. As seen from Figure 6c, the mean SSA values decreased from ~ 0.99 during October (i.e., during the southwest monsoon) to ~ 0.90 during January (i.e., during the northeast monsoon), which is a direct consequence of the increase in absorption coefficient with no significant corresponding increase in the scattering coefficient. The mean and standard deviation of SSA values during SW, transition, and NE monsoon seasons are given in Table 3. The relatively lower SSA during NE monsoon season is due to extensive mixing with polluted air masses containing high absorbing aerosols. The decrease in SSA values and

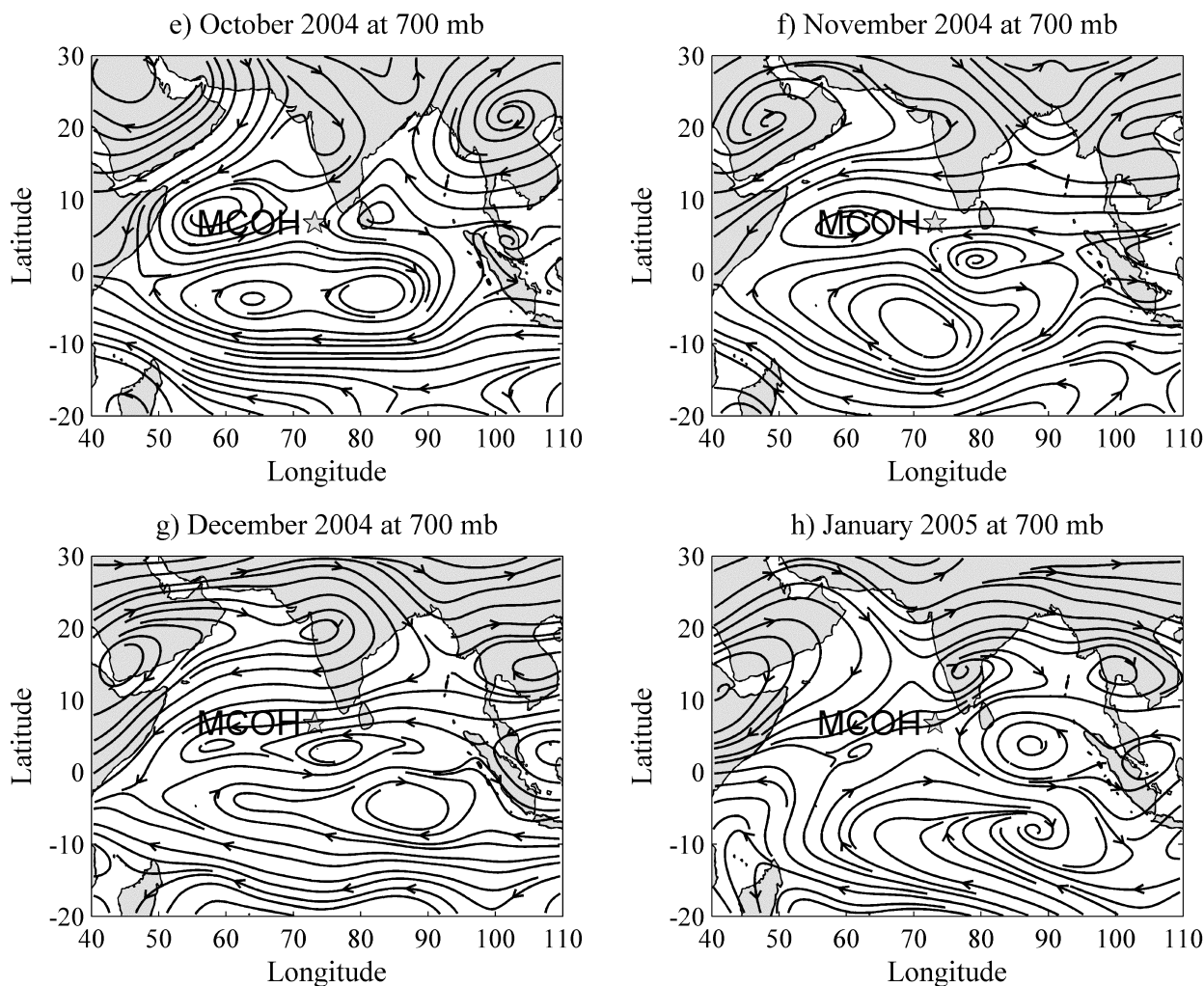


Figure 4. (continued)

the increase in AOD are coincided with wind direction changes (i.e., from southwesterly flow to northeasterly flow), which clearly indicates the arrival of air masses carrying fresh continental pollutants.

4.4. Vertical Profiles of Aerosols

[19] The vertical distributions of aerosols are inferred using the Micro-Pulse Lidar (MPL) data collected during the APMEX campaign. MPL transmits laser pulses at 523.5 nm (green color); the returned signal is analyzed for transit time (range) and intensity of light backscattered by the atmospheric constituents (namely, molecules, aerosols, and clouds). The returned signals include the effects caused by the features of the MPL design. The most important effects include noise included in the detector by the firing of the laser, afterpulse and overlap (which determines the nearest range at which the MPL can accurately image returned signals). The raw returned signals are corrected for these instrumental effects and the data products are processed as described by *Campbell et al.* [2002] and *Welton et al.* [2002]. The aerosol extinction profile is then determined from the calibrated lidar signal assuming an altitude-independent ratio of backscatter to extinction using

the inversion procedure discussed by *Welton et al.* [2000]. The boundary condition of the inversion calculation is set at 8 km and the measured AOD (at 523 nm) is used to calibrate the MPL. The profiles are calculated using cloud free 30-min MPL signal averages.

[20] Figure 7 shows the vertical profiles of aerosol extinction on 9 October 2004 at 1000–1030 UT (dashed line) and on 8 November 2004 at 1030–1100 UT (continuous line). The 9 October profile represents the southwest monsoon period and the 8 November profile represents the transition period (southwesterly to northeasterly flow). On 9 October, the aerosol extinction at the surface is 0.01 km^{-1} and increased to a peak value of 0.03 km^{-1} near the top of the surface mixed layer ($\sim 0.75 \text{ km}$), then decreased to the top height. On 8 November, the aerosol extinction at the surface is 0.01 km^{-1} and increased to a peak value of 0.08 km^{-1} near the top of the surface mixed layer, then decreased until reaching an altitude of $\sim 3 \text{ km}$ with a weak aerosol layers in between. These profiles clearly indicate the increase in the extinction from surface to 3 km altitude by almost three times as the southwest monsoon wanes and transition phase advances. The polluted marine results are shown to be similar to previously published values for

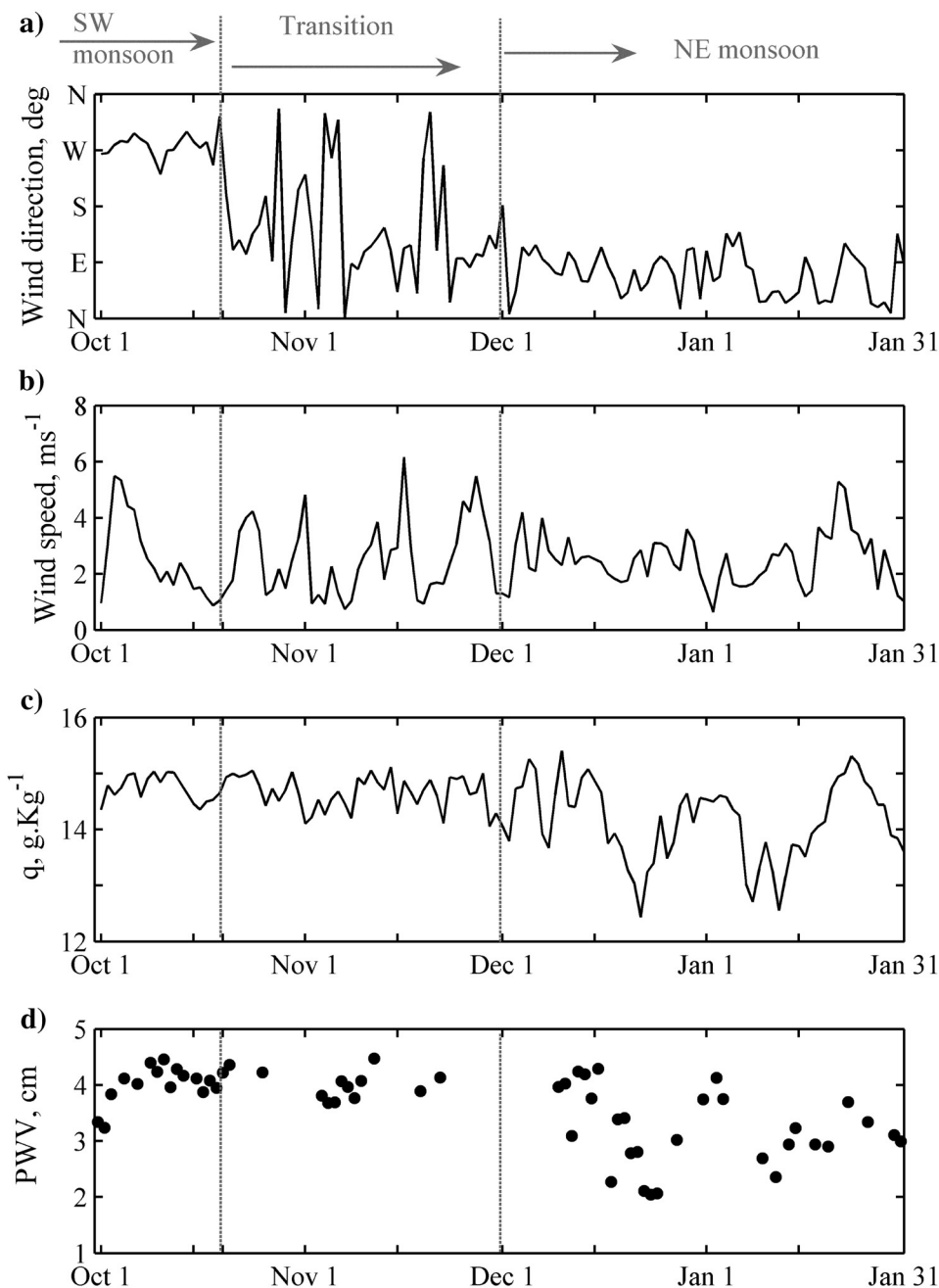


Figure 5. Temporal variation of (a) wind direction in deg, (b) wind velocity in ms^{-1} , (c) specific humidity (q) in g Kg^{-1} , and (d) precipitable water vapor (PWV) in cm from 1 October 2004 to 31 January 2005.

continental aerosols [Ansmann *et al.*, 2000; Welton *et al.*, 2002]. The INDOEX results [Krishnamurthi *et al.*, 1998; Rajeev *et al.*, 2000; Ramanathan *et al.*, 2001] also demonstrated that the northern Indian Ocean is significantly affected by continental pollution during the northeast monsoon season.

5. Comparison of Measured and Calculated Broadband and Visible Surface Solar Fluxes

[21] Before we estimate the aerosol forcing from observations and MACR we must ensure the consistency between the measured aerosol properties and radiation fluxes.

In order to ensure that the observed surface solar fluxes are consistent with measured aerosol properties, we used the 3D Monte Carlo Aerosol Cloud Radiation (MACR) photon transport radiative transfer algorithm described by Podgorny *et al.* [2000], Podgorny and Ramanathan [2001], and Ramanathan *et al.* [2001] and compared observed fluxes with MACR computed fluxes. Here, we determined the agreement between the MACR calculated and measured irradiances to enhance our confidence level in our MACR calculations. The INDOEX aerosol model [Satheesh *et al.*, 1999] is used as input for the MACR calculations, however, certain adjustments are made to incorporate the

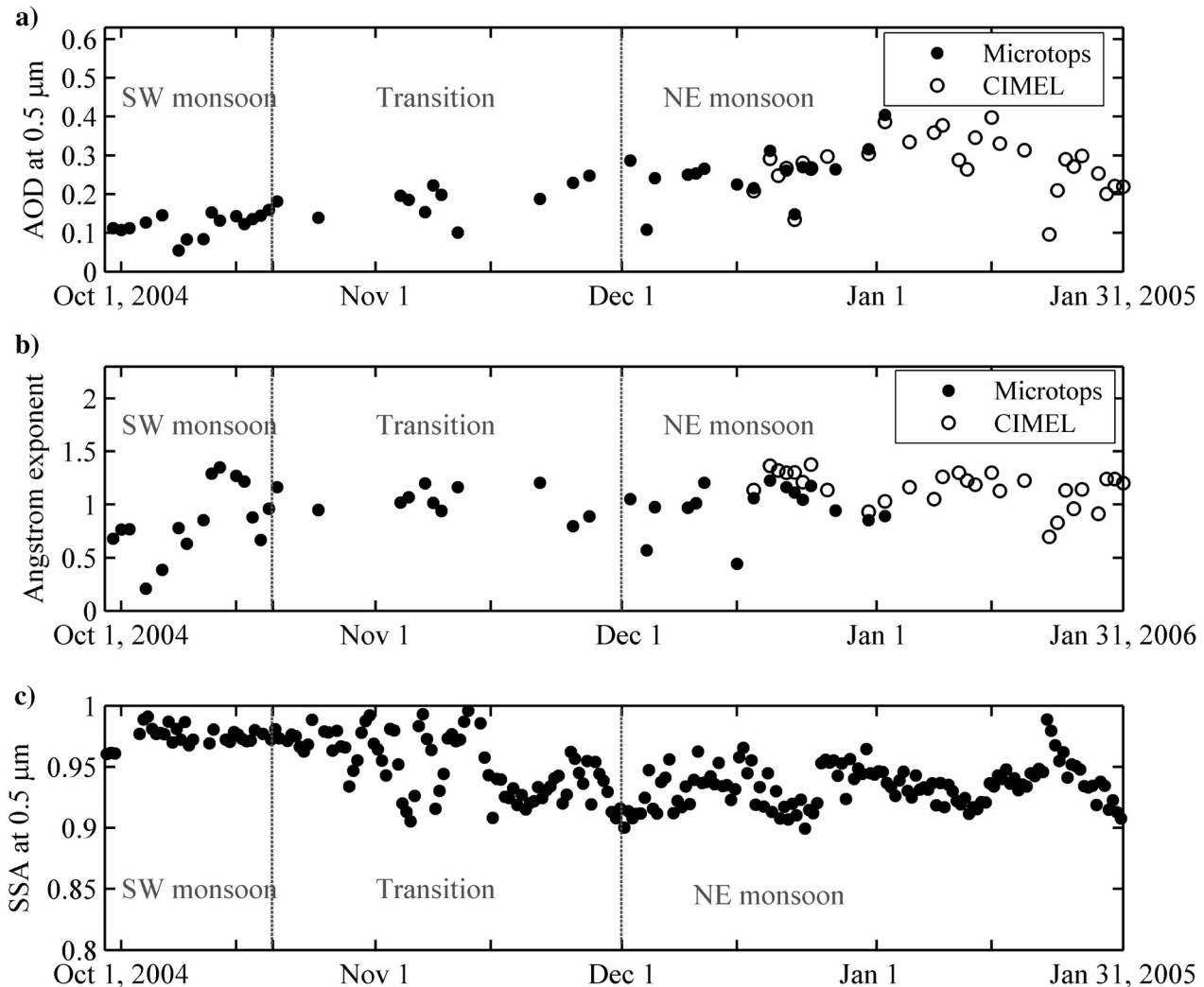


Figure 6. Temporal variation of (a) daily mean aerosol optical depth (AOD) at 500 nm, (b) daily mean Angstrom exponent, and (c) 12-hourly mean aerosol single scattering albedo (SSA) at 500 nm from 1 October 2004 to 31 January 2005.

measured aerosol properties. The cloud-screened, measured spectral AOD, spectral SSA, column water vapor, ozone and solar zenith angle are used as inputs into the MACR. Aerosol single scattering albedo measured at surface level is integrated over the atmospheric column. Aerosol vertical profile obtained from MPL data is used as input to the MACR for October and November data estimates. Because of the lack of MPL data during December and January period, the vertical distribution of aerosol is set as the default exponential profile where the major aerosol concentration is below 3 km. Aircraft measurements during INDOEX have shown that typical height of the aerosol haze layer is below 3 km [Ramanathan *et al.*, 2001]. The tropical standard atmosphere water vapor and ozone profiles [McClatchey *et al.*, 1971] are used in the calculations because of the nonavailability of vertical sounding data. The columnar PWV and ozone in the tropical profiles are respectively 4.09 cm and 253 DU. We scaled the PWV and ozone amounts of the tropical standard atmosphere so that the column amount agrees with measurements. The zenith-angle-

dependent ocean albedo is taken from Briegleb *et al.* [1986]. Following comparison are carried using cloud-screened data points.

[22] Figures 8a–8c show the comparison between measured and MACR calculated surface broadband direct (0.2–4.0 μm), broadband global (0.3–2.8 μm), and visible global (0.4–0.7 μm) irradiances respectively. The comparison shows that MACR calculated surface fluxes are within 2.23, 1.39, and 3.79 Wm^{-2} of the measured surface fluxes for broadband direct, broadband global, and visible global irradiances respectively (respective RMSE, slope and offset are shown in Figures 8a–8c). In general, these small differences between the calculated and measured fluxes are well within instrumental uncertainty and similar differences [Satheesh *et al.*, 1999; Conant, 2000; Podgorny *et al.*, 2000] were documented previously.

[23] We next compare the diffuse fluxes which are a more critical test for the MACR since the aerosols play a dominant role in determining the diffuse fluxes in clear skies. ABC_MCOH has two independent measurements of

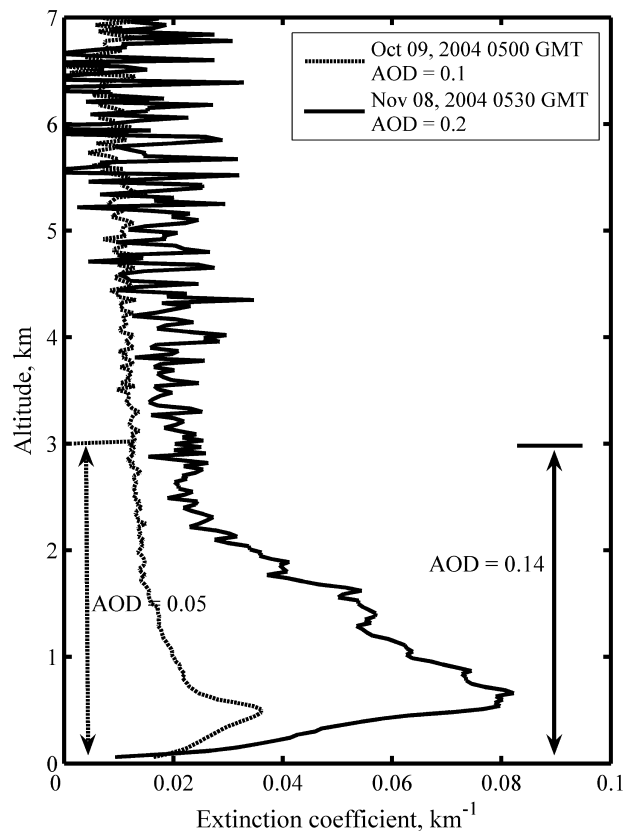


Figure 7. Vertical profiles of aerosol extinction on 9 October 2004 at 1000–1030 UT (dashed line) and on 8 November 2004 at 1030–1100 UT (continuous line). The profiles are calculated using 30-min MPL signal averages.

ground reaching diffuse radiation: (1) diffuse radiation measured by shading the pyranometer and (2) by subtracting the direct solar radiation (pyrheliometer value multiplied with cosine of the solar zenith angle) from the global radiation (unshaded pyranometer). One minor obstacle in constructing the diffuse flux from the second approach is the difference in the spectral region covered by the pyrheliometer and the pyranometer. The pyrheliometer measures the direct radiation in the 0.2–4.0 μm wavelength range, while the unshaded pyranometer measures the global radiation in the 0.3–2.8 μm wavelength range. In order to compare the method 1 and method 2 diffuse fluxes at same wavelength (0.3–2.8 μm), we compared the MACR calculated direct fluxes in the two wavelength regions (0.2–4.0 versus 0.3–2.8 μm). The slope (0.987) and zero offset (–0.990) obtained from this comparison is applied to the measured direct radiation (at 0.2–4.0 μm) to bring it to 0.3–2.8 μm wavelength range. We then subtracted the

direct flux measurements from the global flux measurements to get diffuse flux in the wavelength of 0.3–2.8 μm range.

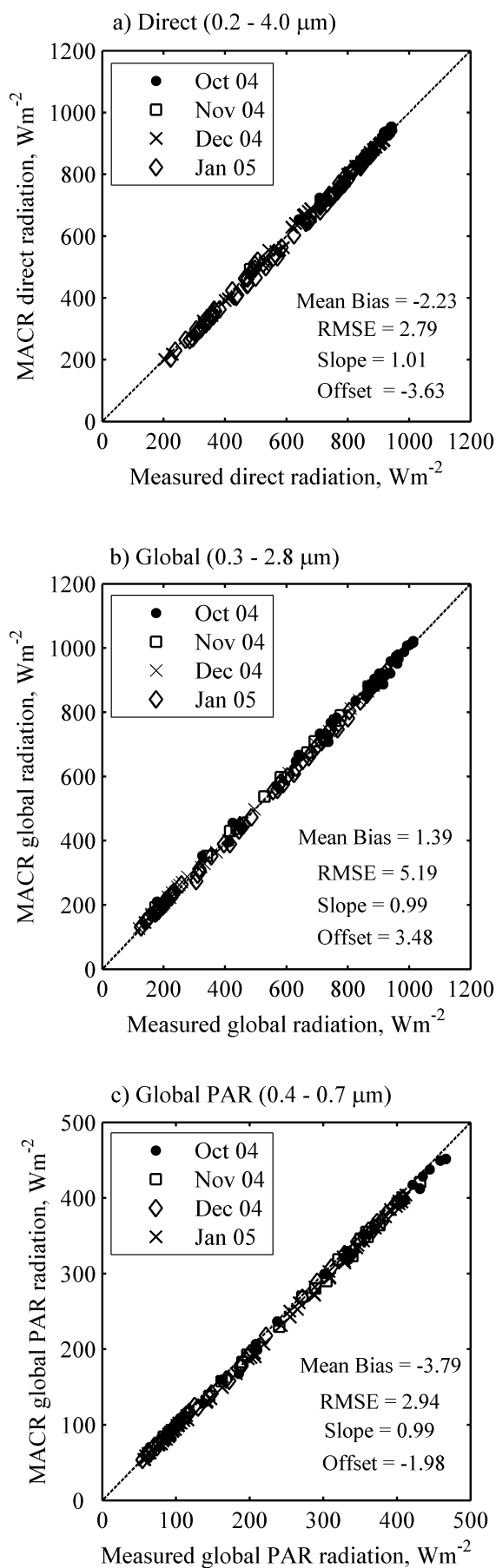
[24] Shown in Figure 9a (solid circle) is the comparison of diffuse flux between method 1 and method 2. Method 1 underestimates the diffuse flux by 6.81 Wm^{-2} (RMSE is 5.69 Wm^{-2} , slope is 0.91 and the zero offset is 4.40 Wm^{-2}) compared to the method 2. This difference could be due to the effect of the shading ball on the measured diffuse flux (shading ball blocks the diffuse radiation coming with angular radius of $\sim 3.2^\circ$) and due to the directional response of the pyranometers at high solar zenith angles. The precise comparison of diffuse fluxes requires a correction in the measured flux (method 1 fluxes) for the portion of diffuse radiation obstructed by the shading ball. The correction for the shading ball is theoretically derived using MACR algorithm by blocking and without blocking the diffuse radiation coming to the forward cone with angular radius of 3.2° in the calculations. We compared these two theoretically calculated diffuse fluxes (MACR diffuse blocked versus MACR diffuse) and the slope (1.07) and zero offset (–0.76) obtained from this comparison is applied to the measured diffuse radiation (method 1) to correct for the shading ball obstruction in the measured diffuse fluxes. The cross symbols in Figure 9a show the comparison between method 2 fluxes and adjusted method 1 fluxes. Diffuse fluxes derived from method 1 agree with those from method 2 within 1.01 Wm^{-2} which builds confidence in the measured diffuse fluxes.

[25] A comparison of the measured and MACR calculated diffuse fluxes are shown in Figure 9b. We used method 2 diffuse flux to compare with MACR calculated diffuse flux. The calculated diffuse flux overestimates the observations by 4.97 Wm^{-2} (RMSE = 4.15 Wm^{-2} , slope = 0.98, offset at zero = 4.05 Wm^{-2}). The differences between calculated and measured fluxes may be due to inherent uncertainties in the input parameters (e.g., AOD, SSA, and water vapor amount), surface reflectance as well as the errors in the flux measurements. Considering the fact that the absolute accuracy of the pyrheliometer and the pyranometer ($\pm 1\%$ and $\pm 2\%$, respectively), the mean bias and RMS errors noted in this comparison are well within the instrumental error and the uncertainties in the input aerosol parameters.

[26] In addition, we compared the MACR calculated diffuse-global flux ratio, which is defined as the downward diffuse irradiance divided by the downward global irradiance, with that measurements to further validate the MACR calculated diffuse fluxes. The ratio of diffuse (diffuse fluxes from method 2) to global solar radiation as estimated from the measurements and from MACR are plotted against corresponding scattering optical depth (AOD_s) in Figure 10. The normalized AOD (normalized with corresponding cosine of the solar zenith angle) is multiplied

Table 3. Mean and Standard Deviation of AOD, Angstrom Exponent, and SSA During Different Phases of Monsoon

Parameter	SW Monsoon (1–19 Oct 2004)	Transition (20 Oct to Nov 2004)	NE Monsoon (Dec 2004 to Jan 2005)
Aerosol optical depth (AOD)	0.12 ± 0.03	0.19 ± 0.04	0.27 ± 0.07
Angstrom exponent	0.86 ± 0.35	1.04 ± 0.14	1.09 ± 0.20
Single scattering albedo (SSA)	0.98 ± 0.01	0.95 ± 0.03	0.93 ± 0.02



with SSA to yield AOD_S . We choose to compare the flux ratio with AOD_S because, in general, the differences in the direct normal irradiance arises because of absorption, while the differences in the downward diffuse irradiance arises because of scattering. The continuous line in Figure 10 is the line of best fit between MACR flux ratio and AOD_S and the symbols represents the measured flux ratio data points. The major impact of aerosols on the diffuse to global ratio is clearly seen in Figure 10, in which the ratio changes from about 0.1 for small AOD_S to as high as 0.7 to large AOD_S . The flux ratios obtained from the measurements and from MACR follow similar trend and are in close agreement. The comparisons between the measured and the calculated fluxes (Figures 8–10) strongly suggest that the measured aerosol properties used in the MACR are consistent with the measured surface fluxes. The agreement between the measured fluxes and calculated values implies that the cloud-free irradiances can accurately be calculated using realistic atmospheric and aerosol properties.

6. Direct Radiative Forcing in the Broadband (0.3–2.8 μm) and in the Visible (0.4–0.7 μm) Band

[27] The aerosol radiative forcing is the effect of aerosol haze (both natural and anthropogenic aerosols) on the net (down minus up) solar flux. The measured data are integrated to yield the aerosol forcing directly from the observations as described by *Ramanathan et al.* [2001] by coupling the aerosol optical depth, chemical and physical properties of aerosols, and the data from the radiometric instruments. We follow the approach proposed by *Satheesh and Ramanathan* [2000] for obtaining the aerosol radiative forcing directly from the radiometric observations. In this approach, the aerosol radiative forcing at the surface and at the top of the atmosphere (TOA) are obtained from observations and the difference between TOA and the surface forcing values defines the atmospheric forcing. The aerosol forcing for cloud-free atmosphere is defined as the difference between the observed cloud-free atmosphere net shortwave radiative flux and the net shortwave radiative flux for the haze-free atmosphere. The forcing efficiency is defined as the rate of change of radiative forcing per unit AOD . The efficiency when multiplied with the AOD yields the aerosol forcing. Here we calculated aerosol radiative forcing at the surface directly from the observations.

6.1. Temporal Variability of Broadband Aerosol Forcing Efficiency

[28] The daily mean net fluxes for cloud-free atmosphere at the surface are obtained on daily basis from 24-hour average of the downward fluxes measured by the pyranometer, subtracting the upward flux calculated using a broadband ocean albedo [*Briegleb et al.*, 1986]. The

Figure 8. Measured versus MACR calculated (a) surface broadband direct fluxes (0.2–4.0 μm), (b) surface broadband global fluxes (0.3–2.8 μm), and (c) surface visible global fluxes (0.4–0.7 μm). The dashed line corresponds to perfect agreement, and the solid circle, square, cross, and diamond symbols represent October, November, December and January data, respectively.

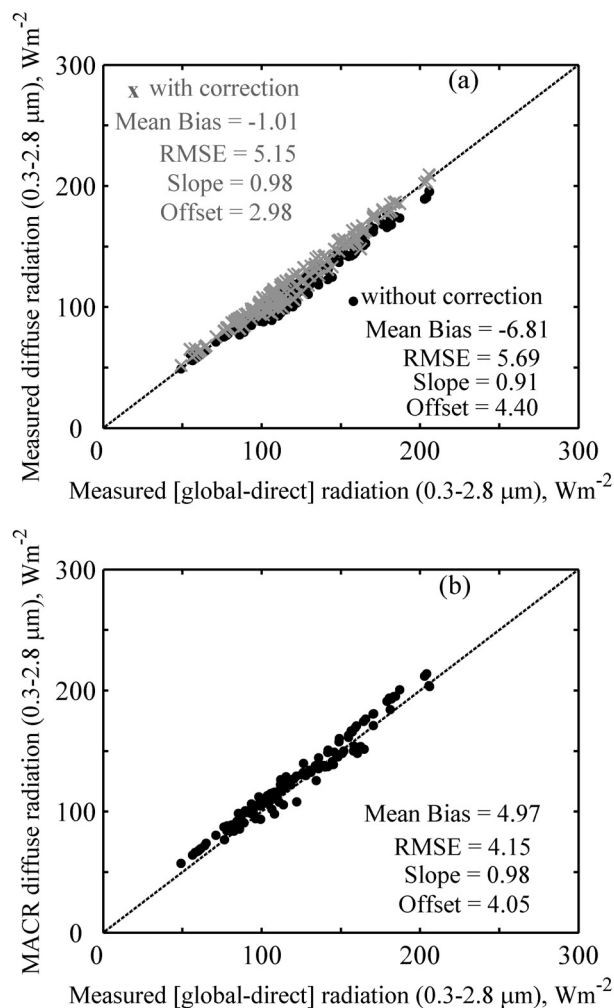


Figure 9. (a) Method 2 (measured [global-direct] radiation) versus method 1 (measured diffuse radiation) surface broadband diffuse radiation. Solid circle indicates the comparison without shading correcting, and cross symbols represent the comparison with shading correction. (b) Method 2 versus MACR calculated surface broadband (0.3–2.8 μm) diffuse fluxes. The dashed line corresponds to perfect agreement. Method 1 and method 2 are explained in the text.

respective diurnally averaged net flux at the surface without aerosol is calculated by the MACR radiative transfer algorithm. The aerosol radiative forcing is calculated by subtracting diurnally averaged net fluxes at surface for the aerosol free condition from the respective measured diurnally averaged daily net fluxes at the surface and is plotted against measured AOD (at 0.5 μm) to yield aerosol forcing efficiency on a monthly basis. Figure 11a shows the daily mean broadband (0.3–2.8 μm) aerosol forcing at the surface as a function of AOD using the data obtained during October, November, December and January periods. The relatively small number of available data points for each month is due to the cloud contamination. The dashed lines in Figure 11a are theoretically (using MACR) calculated aerosol forcing for different values of SSAs (ranges from

1.0 to 0.9) and AOD (ranges from 0 to 0.5 with a 0.05 interval) at 500 nm. The symbols in Figure 11a are measured forcing values from October 2004 to January 2005. The slope, obtained from the linear fit of the forcing from the measurements, is independent of the instruments bias and this slope is termed the aerosol forcing efficiency (aerosol forcing per unit AOD). This estimate of the efficiency provides the average radiative effect of regional aerosol haze. The monthly mean forcing efficiency for the broadband region during October, November, December and January periods are respectively -45 ± 10 , -67 ± 10 , -72 ± 4 and $-70 \pm 4 \text{ Wm}^{-2}$ per unit AOD and are shown in Figure 11b. The mean aerosol forcing efficiency over the tropical Indian Ocean (The Kaashidhoo Climate Observatory in Maldives) during the Northern Hemispheric winter monsoon season (February and March of 1998 and 1999) for the broadband region during INDOEX was -70 to -75 Wm^{-2} per unit AOD [Satheesh and Ramanathan, 2000; Ramanathan et al., 2001; Bush and Valero, 2002], whose values are also shown along with the present values in Figure 11b. Whereas the theoretically calculated aerosol forcing efficiencies for different values of SSA (ranges from 1.0 to 0.9) are -42 , -64 and -80 Wm^{-2} per unit AOD. The measured and theoretically calculated aerosol forcing efficiency values indicate that the depletion of broadband solar radiation by aerosol haze at the Earth's surface for a cloud-free atmosphere is significantly increased by the long-range transport of aerosols during the northeast monsoon.

6.2. Temporal Variability of Visible Aerosol Forcing Efficiency

[29] Solar radiation available for a plant growth occurs in a spectral band from 0.4 to 0.7 μm (visible range) wavelengths and is called Photosynthetically Active Radiation (PAR). In similar to the broadband forcing calculations, the aerosol forcing for the PAR region is calculated and is plotted against AOD in Figure 12a. The dashed lines in the Figure 10a are theoretically (using MACR) calculated aerosol forcing for different values of SSA and AOD at 500 nm. The different symbols in Figure 12a are measured forcing values during

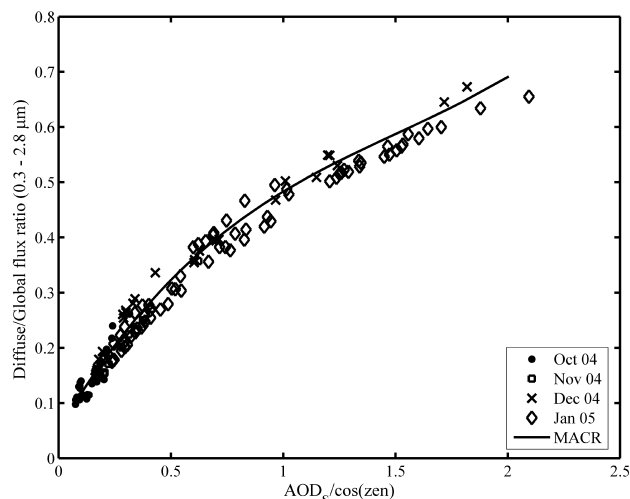


Figure 10. Scatterplot of normalized scattering optical depth (AOD_s) with diffuse-global flux ratio.

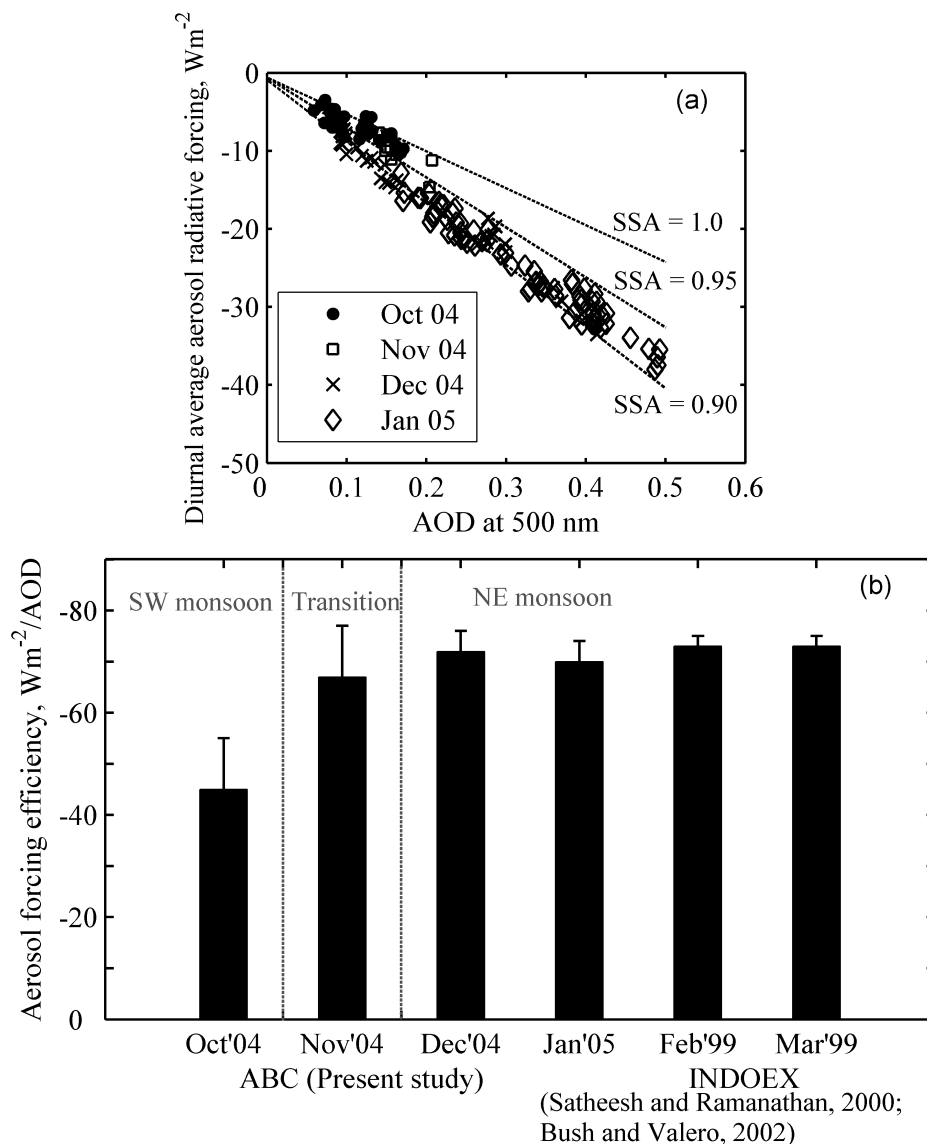


Figure 11. (a) Diurnal average aerosol broadband ($0.3\text{--}2.8\ \mu\text{m}$) radiative forcing at the surface as a function of AOD. The measured data are shown by points. Overlaid dashed lines are theoretical (MACR) radiative forcing calculations with SSAs of 1.0 to 0.9, with 0.05 AOD intervals. (b) Monthly mean aerosol forcing efficiency is obtained as the best linear fit to the respective aerosol forcing values.

October 2004 to January 2005. The monthly mean forcing efficiency from the measurements for the PAR region during October, November, December and January periods are respectively -23 ± 10 , -39 ± 5 , -38 ± 4 and $-37 \pm 4\ \text{Wm}^{-2}$ per unit AOD and are shown in Figure 12b. In comparison, the mean aerosol forcing efficiency over the tropical Indian Ocean during Northern Hemispheric winter season (February and March of 1998) for the PAR region during INDOEX was -35 to $-40\ \text{Wm}^{-2}$ per unit AOD [Conant, 2000], whose values are also plotted in Figure 12b. The MACR calculated aerosol forcing efficiencies for different values of SSA are -22 , -35 and $-44\ \text{Wm}^{-2}$ per unit AOD. Thus the arrival of regional haze from south Asia changes the broadband and visible aerosol forcing efficiencies over the tropical Indian Ocean by a factor of ~ 2

from southwest monsoon (October) to northeast monsoon (January). These values indicate that about $\sim 50\%$ of the forcing occurs in the PAR (visible region of the spectrum).

6.3. Monthly Mean Aerosol Forcing

[30] Monthly mean aerosol forcing is then determined by the monthly mean aerosol forcing efficiency multiplied by the monthly mean AOD and is shown in Figure 13 for the broadband and PAR regions. The monthly mean AOD for October 2004, November 2004, December 2004 and January 2005 are 0.12, 0.17, 0.22, and 0.32 respectively. The mean broadband aerosol forcing observed during October 2004 is $-5\ \text{Wm}^{-2}$ and this value reached $-22\ \text{Wm}^{-2}$ during January 2005, which is associated with the increase in aerosol absorption and optical depth. Whereas, the monthly mean

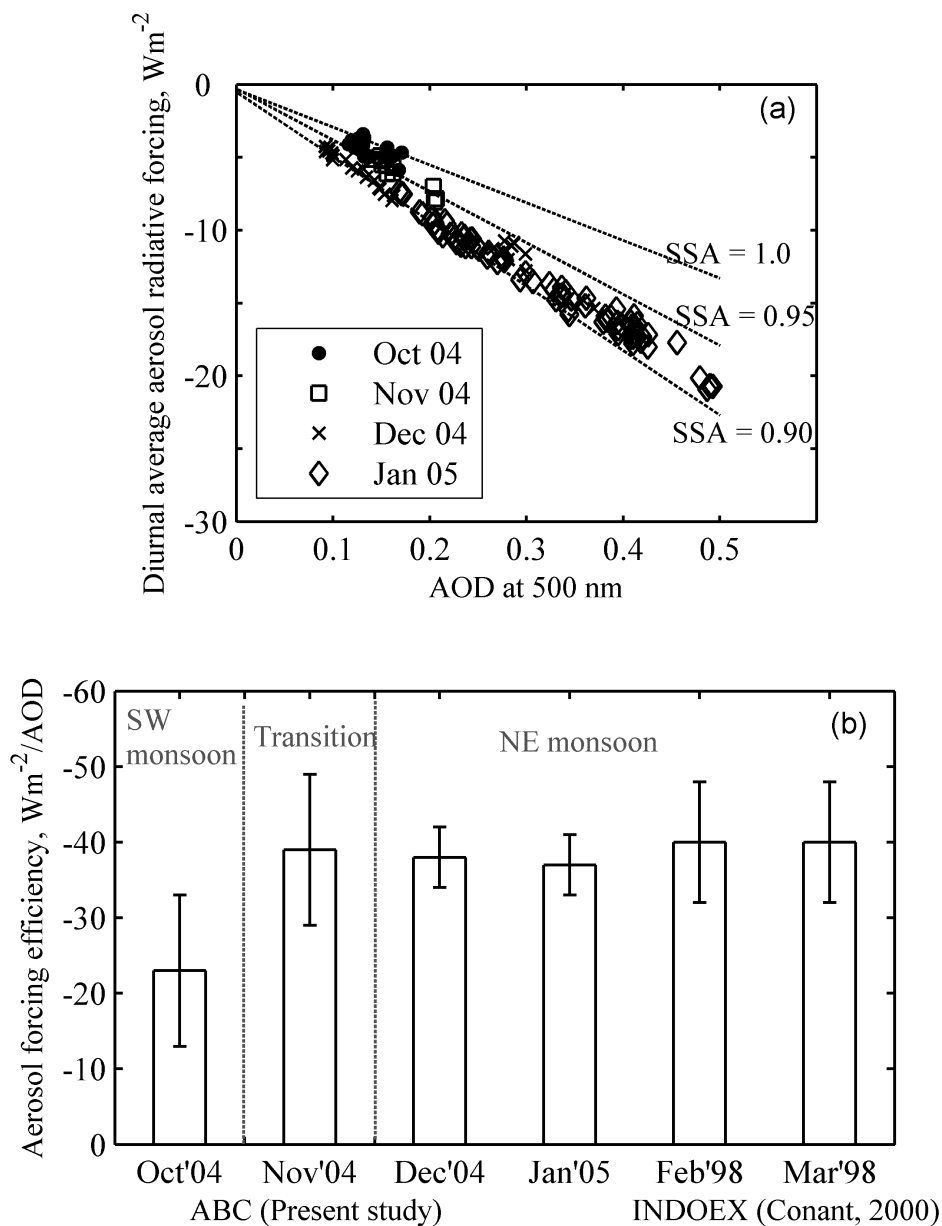


Figure 12. (a and b) Same as Figures 11a and 11b but for the visible range ($0.4\text{--}0.7\ \mu\text{m}$) of the solar spectrum.

aerosol forcing in the visible region during October 2004 is $-3\ \text{Wm}^{-2}$ and this value reached $-12\ \text{Wm}^{-2}$ during January 2005. The INDOEX forcing values during 1999 winter monsoon are also shown in Figure 13. Ramanathan *et al.* [2001] have established the clear sky (cloud-free) aerosol forcing over the Maldives on the basis of observations during the winter (February and March) periods of 1998 and 1999 which showed that the diurnal mean clear sky solar flux decreased by $15\text{--}30\ \text{Wm}^{-2}$ in the broadband region and by $5\text{--}15\ \text{Wm}^{-2}$ in the visible region at the surface. Figure 13 also shows that the seasonal increase in (negative) forcing shown in this study is consistent with the INDOEX observations. Basically the negative aerosol forcing peaks

in March. By April, the flow begins the transition back to the SW monsoon bringing Southern Hemisphere marine air. The surface aerosol radiative forcing in the visible and in the broadband regions is increased by about a factor of four from southwest monsoon to northeast monsoon.

7. Conclusions

[31] As a part of ABC, Maldives Climate Observatory in Hanimaadhoo has been established for long-term measurements of aerosol and radiation over the tropical Indian Ocean. Intensive measurements of aerosol chemical, phys-

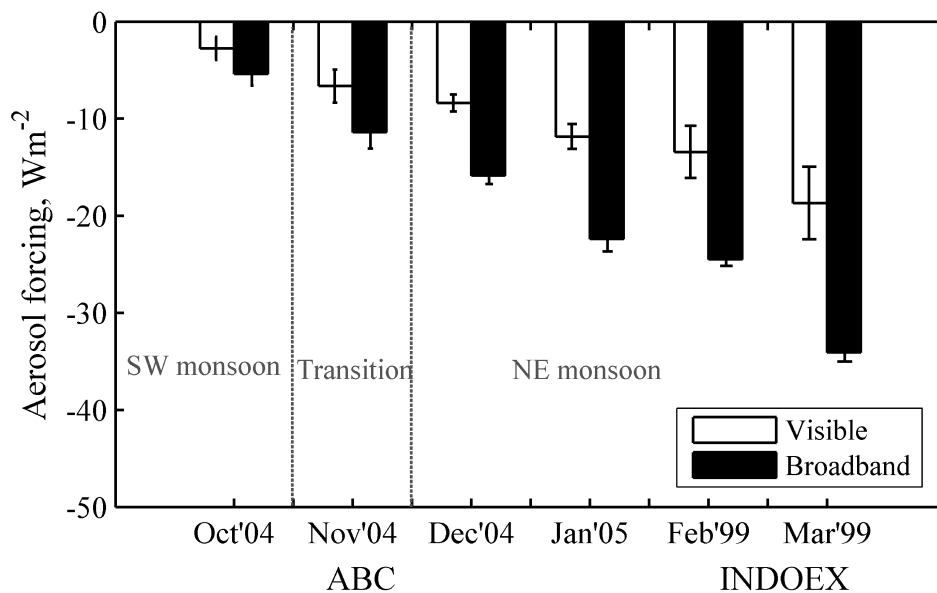


Figure 13. Monthly mean surface aerosol forcing in the broadband region and in the visible region of the solar spectrum.

ical and optical properties simultaneous with measurements of radiative fluxes are made in a real time on a continuous basis since 1 October 2004.

[32] One of our main objectives of the APMEX was to assess the uncertainties in radiometric measurements. We deployed three independent pyrheliometers (Kipp & Zonen and Eppley) to measure the direct solar radiation. Comparison of the three radiometers show the measurement precision to be 3 Wm^{-2} (or 0.5%) with a zero offset of about 0.6 Wm^{-2} (0.1%) or less. The two pyranometers (Kipp & Zonen CM 21 & CM 22) measuring diffuse radiation agree to within $3\text{--}4 \text{ Wm}^{-2}$. We have also compared the diffuse flux measurement methods (diffuse versus global-direct) and these two methods agree within less than 1 Wm^{-2} . The AOD measured directly with two Sun photometers (Microtops and CIMEL) are within 0.02 uncertainty. The MACR model, with input from MCOH data for aerosols, water vapor and ozone, agrees with measured direct, diffuse and global solar fluxes to within $3\text{--}5 \text{ Wm}^{-2}$. The close agreement between the measured fluxes and calculated values implies that the cloud-free irradiances can accurately be calculated using MACR by incorporating realistic atmospheric and aerosol properties. Furthermore the agreement between MACR and measured fluxes to within few reveal the consistency between the measured solar fluxes and the measured aerosol properties.

[33] The measured surface winds demonstrated that the transition from SW to NE monsoon occurs rapidly, within a few days to a week. The southwest monsoon persisted till ~ 19 October 2004. The NE monsoon flow occurred two days after and for the next few weeks the flow switched from SW to NE every few days. By the second week of November the NE flow took over with an occasional relapse to a SW flow. Persistent northeast monsoon was observed from ~ 1 December 2004 onward. Thus this period of

observations provided a unique opportunity to observe and contrast the aerosol forcing of natural aerosols (until third week of October) to anthropogenic aerosols (after November). The AODs are low (~ 0.1) during the southwest monsoon and increased in association with wind direction reversal to a value of ~ 0.4 as northeast monsoon advances. The SSAs are close to 0.99 during the southwest monsoon and decreased to a value of ~ 0.90 during the northeast monsoon. The AOD spectral exponents showed systematic increase in association with the wind direction reversal and suggests the dominance of submicron aerosols. A steady increase in columnar AOD and decrease in SSA are attributed to the arrival of air masses carrying fresh continental pollutants that are characterized by relatively high concentrations of submicron absorbing aerosols. The lidar profile shows the aerosol to be confined to within 3 km during and the aerosol extinction coefficients increased fourfold between surface and about 1.5 km. Thus, from October 2004 (during the southwest monsoon) to January 2005 (during the northeast monsoon flow), the regional aerosol haze changed from relatively pristine (marine origin from south Indian Ocean) to pollution mixed aerosols (continental origin from south and Southeast Asia).

[34] The depletion of solar irradiation by aerosol haze at the Earth's surface in the tropical Indian Ocean is calculated directly from the observations. The cloud-free atmospheric broadband aerosol forcing efficiency is significantly larger in the NE monsoon ($-72 \pm 4 \text{ Wm}^{-2}$ at the surface) compared to the SW monsoon ($-45 \pm 10 \text{ Wm}^{-2}$ at the surface). About 50% of this forcing occurs in the photosynthetically active radiation part of the solar spectrum ($0.4\text{--}0.7 \mu\text{m}$). The broadband and visible aerosol forcing observed during October is -5 and -3 Wm^{-2} respectively. The presence of absorbing aerosols over this region decreased the diurnal mean clear-sky broadband radiation

observed at the surface by as much as 22 W m^{-2} and visible radiation by as much as 11 W m^{-2} , which are about four times to the October values. This large negative forcing at the surface will have significant implications to the hydrological cycle and south Asian climate [Ramanathan et al., 2005].

[35] The observational and model results presented in this study shows how near continuous surface based observations can be used to differentiate the human impact on aerosol forcing from the natural background which is a major challenge for models.

[36] **Acknowledgments.** We acknowledge support from NOAA award NA17RJ1231. Thanks are due to the Republic of Maldives government for coordinating the project ABC in Maldives and for the valuable help of the Maldives Ministry of Environment. The authors also wish to thank Hanimaadhoo island chief for his support during APMEEX. The CIMEL Sun photometer was provided by NASA through the courtesy of Brent Holben of the AERONET group. We acknowledge NOAA-CIRES Climate Diagnostics Center (<http://www.cdc.noaa.gov>) for wind vector data. We thank the reviewers for their helpful comments and suggestions.

References

- Anderson, T. L., and J. A. Ogren (1998), Determining aerosol radiative properties using a TSI 3563 integrating nephelometer, *Aerosol Sci. Technol.*, *29*, 57–69.
- Ansmann, A., D. Althausen, U. Wandinger, K. Franke, D. Müller, F. Wagner, and J. Heintzenberg (2000), Vertical profiling of the Indian aerosol plume with six-wavelength lidar during INDOEX: A first case study, *Geophys. Res. Lett.*, *27*, 963–966.
- Arnott, W. P., K. Hamasha, H. Moosmüller, P. J. Sheridan, and J. A. Ogren (2005), Towards aerosol light-absorption measurements with a 7-wavelength Aethalometer: Evolution with a photoacoustic instrument and 3-wavelength nephelometer, *Aerosol Sci. Technol.*, *39*, 17–29.
- Briegleb, B. P., P. Minnis, V. Ramanathan, and E. Harrison (1986), Comparison of regional clear-sky albedos inferred from satellite observations and model computations, *J. Clim. Appl. Meteorol.*, *25*, 214–226.
- Bush, B. C., and F. P. J. Valero (2002), Spectral aerosol radiative forcing at the surface during the Indian Ocean Experiment (INDOEX), *J. Geophys. Res.*, *107*(D19), 8003, doi:10.1029/2000JD000020.
- Campbell, J. R., D. L. Hlavka, E. J. Welton, C. J. Flynn, D. D. Turner, J. D. Spinhirne, V. S. Scott, and I. H. Hwang (2002), Full-time, eye-safe cloud and aerosol lidar observation at Atmospheric Radiation Measurement Program Sites: Instruments and data processing, *J. Atmos. Oceanic Technol.*, *19*, 431–442.
- Conant, W. C. (2000), An observational approach for determining aerosol surface radiative forcing: Results from the first field phase of INDOEX, *J. Geophys. Res.*, *105*(D12), 15,347–15,360.
- Corrigan, C. E., V. Ramanathan, and J. J. Schauer (2006), Impact of monsoon transition on the physical and optical properties of aerosols, *J. Geophys. Res.*, *111*, D18208, doi:10.1029/2005JD006370.
- Dubovik, O., A. Simrnov, B. N. Holben, M. D. King, Y. J. Kaufman, T. F. Eck, and I. Slutsker (2000), Accuracy assessment of aerosol optical properties retrieved from Aerosol Robotic Network (AERONET) Sun and sky radiance measurements, *J. Geophys. Res.*, *105*, 9791–9806.
- Dubovik, O., B. N. Holben, T. F. Eck, A. Smirnov, Y. J. Kaufman, M. D. King, D. Tanre, and I. Slutsker (2002), Variability of absorption and optical properties of key aerosol types observed in worldwide locations, *J. Atmos. Sci.*, *59*, 590–608.
- Eck, T. F., B. N. Holben, O. Dubovik, A. Smirnov, I. Slutsker, J. M. Lobert, and V. Ramanathan (2001), Column-integrated aerosol optical properties over the Maldives during the northeast monsoon for 1998–2000, *J. Geophys. Res.*, *106*, 28,555–28,566.
- Holben, B. N., et al. (1998), AERONET—A federated instrument network and data archive for aerosol characterization, *Remote Sens. Environ.*, *66*, 1–16.
- Ichoku, C., et al. (2002), Analysis of the performance characteristics of the five-channel Microtops II Sun photometer for measuring aerosol optical thickness and precipitable water vapor, *J. Geophys. Res.*, *107*(D13), 4179, doi:10.1029/2001JD001302.
- Kripalani, R. H., and P. Kumar (2004), Northeast monsoon rainfall variability over south peninsular India vis-à-vis the Indian Ocean dipole mode, *Int. J. Climatol.*, *24*, 1267–1282.
- Krishnamurthi, T. N., B. Jha, J. M. Prospero, A. Jayaraman, and V. Ramanathan (1998), Aerosol and pollutant transport over the tropical Indian Ocean during the 1996 northeast monsoon and the impact on radiative forcing, *Tellus, Ser. B*, *50*, 521–542.
- Kumar, K. K., K. R. Kumar, R. G. Ashrit, N. R. Deshpande, and J. W. Hansen (2004), Climate impacts on Indian agriculture, *Int. J. Climatol.*, *24*, 1375–1393.
- McClatchey, R. A., R. W. Fenn, J. E. A. Selby, F. E. Volz, and J. S. Garing (1971), Optical properties of the atmosphere, *Rep. AFCRL-TR-71-0279*, *Environ. Res. Pap.*, *354*, Air Force Cambridge Res. Lab., Bedford, Mass.
- Morys, M., F. M. Mims III, S. Hagerup, S. E. Anderson, A. Baker, J. Kia, and T. Walkup (2001), Design, calibration, and performance of Microtops II handheld ozone monitor and Sun photometer, *J. Geophys. Res.*, *106*, 14,573–14,582.
- Podgorny, I. A., and V. Ramanathan (2001), A modeling study of the direct effect of aerosols over the tropical Indian Ocean, *J. Geophys. Res.*, *106*(D20), 24,097–24,105.
- Podgorny, I. A., W. C. Conant, V. Ramanathan, and S. K. Satheesh (2000), Aerosol modulation of atmospheric and solar heating over the tropical Indian Ocean, *Tellus, Ser. B*, *52*, 947–958.
- Rajeev, K., V. Ramanathan, and J. Meywerk (2000), Regional aerosol distribution and its long-range transport over the Indian Ocean, *J. Geophys. Res.*, *105*, 2029–2043.
- Ramanathan, V., and P. J. Crutzen (2003), New directions: Atmospheric brown clouds, *Atmos. Environ.*, *37*, 4033–4035.
- Ramanathan, V., and M. V. Ramana (2003), Atmospheric brown clouds: Long-range transport and climate impacts, *EM*, *12*, 28–33.
- Ramanathan, V., et al. (2001), The Indian Ocean Experiment: An integrated analysis of the climate forcing and effects of the great Indo-Asian haze, *J. Geophys. Res.*, *106*, 28,371–28,398.
- Ramanathan, V., C. Chung, D. Kim, T. Bettge, L. Buja, J. T. Kiehl, W. M. Washington, Q. Fu, D. R. Sikka, and M. Wild (2005), Atmospheric brown clouds: Impacts on South Asian climate and hydrological cycle, *Proc. Natl. Acad. Sci. U. S. A.*, *102*, 5326–5333.
- Satheesh, S. K., and V. Ramanathan (2000), Large differences in tropical aerosol forcing at the top of the atmosphere and Earth's surface, *Nature*, *405*, 60–63.
- Satheesh, S. K., V. Ramanathan, X. Li-Jones, J. M. Lobert, I. A. Podgorny, J. M. Prospero, B. N. Holben, and N. G. Loeb (1999), A model for the natural and anthropogenic aerosols for the tropical Indian Ocean derived from Indian Ocean Experiment data, *J. Geophys. Res.*, *104*, 27,421–27,440.
- Spinhirne, J. D., J. Rall, and V. S. Scott (1995), Compact eye-safe lidar systems, *Rev. Laser Eng.*, *23*, 26–32.
- Welton, E. J., et al. (2000), Ground-based lidar measurements of aerosols during ACE-2: Instrument description, results, and comparison with other ground-based and air-borne measurements, *Tellus, Ser. B*, *52*, 635–650.
- Welton, E. J., K. J. Voss, P. K. Quinn, P. J. Flatau, K. Markowicz, J. R. Campbell, J. D. Spinhirne, H. R. Gordon, and J. E. Johnson (2002), Measurements of aerosol vertical profiles and optical properties during INDOEX 1999 using micropulse lidars, *J. Geophys. Res.*, *107*(D19), 8019, doi:10.1029/2000JD000038.

M. V. Ramana and V. Ramanathan, Center for Atmospheric Sciences, Scripps Institution of Oceanography, University of California, San Diego, 9500 Gilman Drive, La Jolla, CA 92093, USA. (ramana@fiji.ucsd.edu)